# The role of coronal mass ejections and interplanetary shocks in interplanetary magnetic field statistics and solar magnetic flux ejection

Charles W. Smith
Bartol Research Institute, University of Delaware, Newark

John L. Phillips
Los Alamos National Laboratory, Los Alamos, New Mexico

## Abstract

We examine the role of coronal mass ejections (CMEs) and interplanetary shocks in modifying the large-scale winding of the interplanetary magnetic field (IMF) by extracting CME and shock observations from the ISEE 3 data set and analyzing periods of the disturbed and undisturbed solar wind separately. We use the full ISEE 3 data set representing the entire $L_1$ mission (1978 – 1982). We conclude that CMEs, the shocks upstream of CMEs, and other interplanetary shocks are responsible for the apparent overwinding of the IMF spiral relative to the Parker prediction. The IMF winding angle asymmetry is preserved following the removal of the interplanetary disturbances. We also examine the IMF components, the IMF magnitude and the solar wind speed, and the dependence of those averages and asymmetries on CMEs and shock disturbances. An estimate is obtained for the anomalous azimuthal field contained within CMEs which apparently results from the closed-field topology. We provide new evidence for a nonzero field component crossing the heliospheric current sheet. Last, we examine the role of CMEs and shocks in the measurement of solar magnetic flux ejection. We provide estimates for the average amount of flux transported by CMEs and the error in flux transport analyses that include shock data, and we examine the possible north-south asymmetry of the flux.

## 1. Introduction

Past studies of the spiral winding of the interplanetary magnetic field (IMF) using the National Space Science Data Center's (NSSDC) omnitape data set as well as Pioneer-Venus Orbiter and Voyager observations have revealed an overwinding relative to the *Parker* [1958] prediction. On average, the difference between the observed and predicted winding angle as computed from the omnitape data set is $1.5° \pm 0.5°$ [*Smith and Bieber*, 1991, 1992]. Neither uncertainties in the source surface height nor reasonable variation of the solar rotation rate at that surface can account for the observations.

An asymmetry between the winding of the northern and southern hemispheres has also been observed [*Bieber*, 1988; *Smith and Bieber*, 1992, 1993; Sabbah, 1995, 1996]. The IMF north of the heliospheric current sheet is generally more tightly wound than the field south of the current sheet. Analysis of the omnitape data set reveals this difference as $2.4° \pm 0.8°$ at the Earth's orbit for the years 1965 through 1987 [*Smith and Bieber*, 1993]. Analysis of the Pioneer-Venus Orbiter observations reveals similar behavior at 0.7 AU [*Smith and Bieber*, 1993]. Both the overwinding and the asymmetry persist over many years and are statistically significant. Both results have implications for cosmic ray propagation in the heliosphere.

These past analyses suggest that the apparent overwinding is greatest during times of solar magnetic reversal and heightened solar activity when interplanetary disturbances such as coronal mass ejections (CMEs) and interplanetary shocks are most frequent. Simple association suggests the possibility that these disturbances may account for the overwinding of the IMF. By examining the ISEE 3 data set from the years 1978 through 1982, we include the years of solar maximum surrounding the 1980 magnetic solar reversal when the overwinding was greatest. No enhancement in the asymmetry is associated with times of peak solar activity. In fact, the years of greatest asymmetry occur during solar minimum [*Bieber*, 1988; *Smith and Bieber*, 1993].

The *Parker* [1958] theory is a steady state prediction that avoids discussion of transient structures such as CMEs and shocks. Interplanetary dynamical processes such as overtaking high-speed streams, CME propagation into the undisturbed medium, and shock processing of the interplanetary plasma are outside this description and contribute to the statistics in a manner that a steady state theory cannot describe. It is possible that the resulting alterations in the IMF are asymmetrical about the predicted field orientations or that the sampling of these regions is not evenly distributed and that this possibility may account for the overwinding and asymmetry observations.

The presence of bidirectional streaming suprathermal electrons has been used as an indicator of closed magnetic structures, interpreted as CMEs [e.g., *Gosling et al.*, 1987]. The characteristics of the counterstreaming beams suggest that most CMEs remain magnetically attached to the Sun at Earth's orbit, rather than disconnecting into closed plasmoids [*Phillips et al.*, 1992]. Many CMEs have flux rope magnetic structures suggesting partial disconnection from the corona [e.g., *Gosling*, 1990]. Regardless of their specific field topologies, the closed fields associated with CMEs constitute structures outside the Parker description of the IMF. Deflection and draping of the IMF both upstream and downstream of these structures also produce deviations from the Parker description [e.g., *McComas et al.*, 1989].

Shocks form in the solar wind due to a variety of sources including the propagation of CMEs and may be either forward or reverse. Compression of the plasma across the shock causes the downstream field to be more nearly perpendicular to the shock normal and may result in an apparent overwinding of the IMF statistics.

*Weber and Davis* [1967, 1970] considered the effects of angular momentum in the winding of the IMF and concluded that an azimuthal wind speed which diminishes with heliocentric distance would allow the winding of the IMF to approach the Parker prediction by $\sim$ 1 AU. We have considered this effect in preparation for the study presented here, and it has been dismissed as a possible explanation for both the overwinding and the asymmetry of the IMF. A simple examination of the theory presented by *Weber and Davis* [1967, 1970] will convince the reader that the considerations described therein cannot be expected to produce an overwinding or asymmetry of the magnitude reported here or by previous studies.

In the following sections we first examine the distribution of CMEs and shocks within the ISEE 3 data set, taking note of the relative frequency of occurence of the disturbances and their position relative to the current sheet. In section 3 we examine the role of CMEs and shocks in the computation of winding angle statistics at Earth orbit. Following this we examine the statistical properties of the IMF intensity, the wind speed, and the magnetic field components, and we estimate the average azimuthal field within CMEs at the point where they are launched into the solar wind. In section 4 we examine the role of disturbances in the related evaluation of solar magnetic flux ejection. We close with a brief discussion.

## 2. ISEE 3 at $L_1$

ISEE 3 spent approximately 51 months (from August 1978 through October 1982) upstream of Earth at the $L_1$ libration point. This places the spacecraft ahead of the foreshock in solar wind plasma that is largely undisturbed by the presence of Earth. A catalog of CME and shock times for this data set has already been compiled [e.g., *Phillips et al.*, 1993].

That catalog lists 179 CME observations, 82 forward shocks upstream of or within the CMEs, 85 forward shocks unassociated with any obvious CME event (we will call these "non-CME" shocks), and 4 reverse shocks. A significant fraction of the non-CME forward shocks are thought to be driven by corotating interaction regions (CIRs), while the rest are probably driven by CMEs that were not directly sampled by ISEE 3. Most CIRs do not have observable reverse shocks at 1 AU. The few reverse shocks actually identified were weak. For these reasons, we have disregarded reverse shocks in this analysis.

The top panel of Figure 1 shows the number of CMEs recorded within the catalog per solar rotation as computed from the synodic period. CME activity is particularly high during 1980 (the year of magnetic solar reversal) and the 2 years following which coincide with the same general time when the overwinding of the IMF appears greatest. The bottom panel of Figure 1 shows the percentage of time for each solar rotation that the spacecraft spends within CMEs. It is not unusual for CMEs to comprise 20% or more of the data for a given 27-day period.

During the 3 1/2 years in question, CMEs alone represent 8% of the data. CMEs together with their upstream shocks represent 10%. Non-CME shocks represent another 6%

of the data if 24 hours of data are included following each shock to account for the processed plasma and twice this if 48 hours are included.

By examining the 24-hour period before and after each disturbance, we can assign a toward or away sector identity to the location of each disturbance based on the dominant polarity of the interval. In turn, that interval can be denoted as being either north or south of the current sheet as determined by the solar polarity. Excluding the year 1980 when the changing solar polarity precludes the determination of the spacecraft's location either north or south of the heliospheric current sheet on the basis of sector polarity, CMEs are nearly equally divided between the two hemispheres with 58 north and 55 south of the current sheet. Likewise, the non-CME shocks are divided 35 north of the current sheet and 34 south.

## 3. Overwinding and Asymmetry

We repeat the earlier examinations of the overwinding and asymmetry of the IMF spiral windings using ISEE 3 data from the $L_1$ mission. Five-minute data resolution is used to better resolve the passage of disturbances. The catalog of CME and shock observations is used to remove or focus upon these disturbances in an effort to determine if they have been a significant contributor to the previously observed winding angle statistics.

The ISEE 3 data are defined in heliocentric $(R, T, N)$ coordinates (where $\hat{\mathbf{R}}$ is directed radially outward from the Sun to the spacecraft, $\hat{\mathbf{T}}$ is the tangential component which is coplanar with the Sun's rotational equator and directed in the sense of Earth's orbital motion, and the normal component is given by $\hat{\mathbf{N}} = \hat{\mathbf{R}} \times \hat{\mathbf{T}}$). We represent the measured field components by $(B_R, B_T, B_N)$.

Each 5-min data point is assigned a sector identity according to its orientation relative to the predicted spiral winding angle computed using the observed solar wind speed and setting the source surface radius to zero (the upper limit estimate of the winding angle prediction). That prediction is given by

$$\tan(\Psi^{(P)}) \equiv \frac{2\pi r \sin(\Theta)}{V_{sw} T} \left[1 - \frac{b}{r}\right] \qquad (1)$$

where $\Psi^{(P)}$ is the *Parker* [1958] prediction for the winding angle, $r$ is the heliocentric distance, $\Theta$ is the polar angle, $V_{sw}$ is the solar wind speed, $T$ is the sidereal period which we take to be 25.4 days, and $b$ is the source surface radius. Equation (1) assumes that the wind originates from the same solar latitude as where the observation is made. An actual origin at higher latitude where the solar rotation is slower would produce an underwinding, not an overwinding. A similar result can be derived for the conservation of angular momentum [*Smith and Bieber*, 1996].

Estimates of $b$ range between 1 and 20 $R_S$. This gives values for $\Psi^{(P)}$ at Earth's orbit that vary by $\sim 0.14°/R_S$. We will take $b = 0$, which maximizes the predicted winding angle and minimizes the opportunity for overestimating the overwinding. When ISEE 3 proton data are no longer available for the computation of the wind speed, electron data are substituted. Average field values for toward and away sectors are computed for each solar rotation, and these values are treated as independent estimates of the means for each sector type or hemisphere. This avoids finite correlation length problems associated with treating each 5-min measurement as a statistically independent estimate [*Forbush et al.*, 1982, 1983; *Bieber*, 1988]. From the ensemble

of means computed over individual solar rotations, the error in the mean is computed and cited as the uncertainty. Where desired the phase of the solar cycle is factored into the analysis so that sector types can be associated with the location of the spacecraft either north or south of the current sheet [*Rosenberg and Coleman*, 1969]. In this way, hemispheric asymmetries can be computed [*Bieber*, 1988] with toward (away) sectors regarded as indicative of a spacecraft location south (north) of the current sheet prior to 1980 and north (south) of the current sheet after 1980. Non-CME shocks are extended by a prescribed time following the shock's passage in an attempt to represent the extent of the shock's influence on the plasma.

As with *Smith and Bieber* [1992, 1993] we insist that each sector type be represented by at least 100 hours of possibly noncontiguous data for each solar rotation or that rotation is discarded from the analysis. The 100-hour condition is arbitrary, but this insures that sufficient coverage is achieved to compute a meaningful average for the quantities. Because the year 1980 is a time of changing solar magnetic state, we disregard this year in the following analysis.

Table 1 defines the various subsets of the data set used in this analysis. The entire ISEE 3 data set, excluding 1980, is first run for reference followed by subsets of the entire data set which are defined by what was removed from the data set and excluded from the analysis: removing only CMEs, CMEs extended to include the upstream shock, CMEs extended to include the upstream shock with an additional 24 hours following the CME removed, non-CME shocks with 24 hours following the shock, the same with 48 hours following the shock, and, last, all of the above. In some instances the disturbance intervals are examined directly. When this is done, it is necessary to suspend the 100-hour condition.

Shock-to-CME separation at 1 AU can for some events exceed 24 hours, although the average value is roughly 13 hours [*Gosling et al.*, 1987]. The duration of shock- or wave-processed plasma associated with CIRs at 1 AU is not well documented nor is the duration for CME-driven events in which the CME is not directly observed. We have chosen two postshock intervals, 24 and 48 hours, as a conservative approach to eliminating shock-processed solar wind. Some unshocked solar wind is usually included in the 48 hours following the shock's passage and probably in the first 24 hours as well.

### 3.1. Winding Angle Statistics

Table 2 lists the basic results for our analysis of the overwinding of the IMF and north-south winding angle asymmetry and updates the preliminary results of *Smith and Phillips* [1996]. A positive asymmetry indicates a greater winding angle north of the current sheet than south of it. Both the overwinding and the asymmetry analyses are based upon the scalar comparison of the winding angles for each 5-min interval. The overwinding compares these values with the predicted winding angles derived from (1). Both of these methods are described by *Smith and Bieber* [1991, 1993]. The overwinding result for all data is in good agreement with the omnitape analysis of *Smith and Bieber* [1991] for these years. The observed reduction in the overwinding as the various disturbances are removed indicates that CMEs, the region between the CME and the upstream shock, and the regions downstream of non-CME shocks account for all of the overwinding of the IMF.

The asymmetry is largely unaffected by the removal of the disturbances. The presence of

an asymmetry is only a $1\sigma$ result, so our ability to make conclusive judgements regarding the role of the disturbances in past analyses is limited. However, the asymmetry is in good agreement with the past analysis of the omnitape for these same years [*Smith and Bieber*, 1993]. This same past analysis shows that the asymmetry is small during times of greatest CME activity, which is consistent with there being another source for this observation. The survival of the asymmetry following the removal of the disturbances in the ISEE 3 data set offers further support for an alternate source.

An overwinding and asymmetry for the CMEs themselves can also be computed if we dispense with the 100-hour restriction. In that case, the computed overwinding of the field within the CMEs is $8.7° \pm 2.8°$, while the computed asymmetry is $15.0° \pm 10.2°$. Addition of the CME-associated shocks and the non-CME shocks with 24 hours of trailing data brings these values down to $7.4° \pm 2.1°$ and $6.7° \pm 5.8°$, respectively.

The top panel of Figure 2 shows the distribution for the difference between the observed winding angle and the predicted winding angle derived from the observed wind speed and the *Parker* [1958, 1963] theory for the entire ISEE 3 data set. As shown previously for the omnitape data set [*Smith and Bieber*, 1991, 1992], the distribution of observed winding angles is shifted to larger values relative to the Parker prediction. The bottom panel of Figure 2 shows the distribution for the difference between the observed and predicted winding angles for the undisturbed data intervals (top curve) and the disturbed data containing CMEs and shocks (bottom curve). The disturbances are made up of CMEs extended to include the upstream shock and non-CME shocks plus the following 48 hours. Undisturbed data consist of all other measurements and correspond to the bottom row of Table 1. While the shift to greater winding angles than predicted is no longer evident in the undisturbed data, the disturbed data clearly show a shift to greater values of the winding angle than the Parker theory predicts.

### 3.2. Field Magnitude Statistics

It is interesting to apply the same analysis method to the IMF intensity. Table 3a contains the average intensity of the 5-min averages of the magnetic field as contained in the ISEE 3 data set and computed for the various subsets already discussed. This is not the intensity of the vector-averaged field but is instead the scalar average of the individual intensities. The average IMF intensity decreases by $\sim 8\%$ as the various disturbances, including CMEs, are removed from the data set. This is a $3\sigma$ result and is expected due to the reported observations of high field intensities within CMEs [e.g., *Gosling et al.*, 1987]. The implication is that statistics of quantities which rely on the intensity of the IMF place an emphasis on the high-field regions of CMEs and shocked plasma. This does not include the winding angle statistics shown in Table 2 since those results are based on scalar analyses. The asymmetry of the magnetic field intensity is small, but there is a hint that the asymmetry is increasingly negative as the disturbances are removed.

Table 3b shows the average field intensity and asymmetry for the disturbances. The elevated field intensity of CMEs and shock data relative to the undisturbed solar wind is demonstrated. The asymmetry of the IMF intensity for CMEs appears to be a small but statistically significant result at $\sim 4\%$ of the average IMF intensity in support of the asymmetry inference above. The north-

ern disturbances have more intense fields than the southern disturbances. Extension of the non-CME shocks to include the following 24 hours yields an average field intensity similar to that of the CMEs, but the asymmetry is no longer significant. The enhanced field intensity downstream of the CME-related shocks is also evident.

### 3.3. Wind Speed Statistics

*Bieber* [1988] and *Smith and Bieber* [1993] raised the possibility that a north-south asymmetry in the wind speed could account for the winding angle asymmetry. Those authors found insufficient wind speed asymmetry to account for the observed winding angle asymmetry. Likewise, *Gazis* [1995] has argued that a north-south asymmetry of the wind speed could explain observations of apparent solar wind deceleration in the outer heliosphere reported by *Richardson et al.* [1995].

Table 4a shows the average wind speed and wind speed asymmetry for the various data subsets shown in Table 1. As before, averages over solar rotations are computed to represent statistically independent samplings of the data. The mean, difference, and errors are computed from these intermediate-scale values. Although the average wind speed decreases as CMEs and other disturbances are removed from the dataset, it is remarkable how little the average wind speed changes. For instance, the average wind speed decreases by only 1.3 $km \cdot s^{-1}$ when CMEs are removed. Since CMEs represent about 8% of the total data set, they must average only about 16 $km \cdot s^{-1}$ greater wind speed than the rest of the observations.

Direct analysis of the average wind speed of CMEs confirms this inference if we again suspend the 100-hour rule. The average wind speed for CMEs is $443.2 \pm 11.1$ $km \cdot s^{-1}$, 16.2 $km \cdot s^{-1}$ greater than the average of the entire data set and 22.2 $km \cdot s^{-1}$ greater than the average wind speed for the undisturbed solar wind as represented by combined subset 2. This result and the wind speed statistics of several disturbance subsets are listed in Table 4b. This average CME speed at Earth's orbit is 27 $km \cdot s^{-1}$ less than the 470 $km \cdot s^{-1}$ average seen in white light coronagraph data taken from Skylab [*Gosling et al.*, 1976]. Inclusion of the solar wind plasma between the CME and the upstream shock raises the average wind speed by an additional 11.9 $km \cdot s^{-1}$ which implies that the CME-to-shock plasma, and probably the leading edge of the CME as well, are moving at a greater speed than the remainder of the CME. This would suggest a radial expansion of the structure with time that is still ongoing at Earth orbit [*Gosling*, 1990]. The 24 hours of data following non-CME shock disturbances display an average wind speed that is 22.3 $km \cdot s^{-1}$ greater than the average wind speed of CMEs. This is reduced to 4.7 $km \cdot s^{-1}$ when the 48 hours following non-CME shocks are used (not shown), which demonstrates how quickly the driving plasma behind interplanetary shocks decreases in speed over the associated 2-day length scale.

The wind speed asymmetry shown in Tables 4a and 4b is only 3 to 7 $km \cdot s^{-1}$. This is especially remarkable to the extent that the wind observed at Earth orbit originates from two separate and opposing polar holes which appear to have very nearly identical solar wind characteristics in so far as this data set is concerned. Although only a $1\sigma$ result, the observed wind speed for undisturbed data is greater north of the heliospheric current sheet than south of it, in general agreement with Pioneer-Venus Orbiter and omnitape observations [*Smith and Bieber*, 1993] but in dis-

agreement with the inferences of *Gazis* [1995] drawn from Voyager 2 observations in the outer heliosphere. The present result also agrees qualitatively with 1994–1995 observations from the Ulysses pole-to-pole transit [*Goldstein et al.*, 1996], despite the time difference of 1.5 sunspot cycles. The north-south asymmetry of the CME wind speed shown in Table 4b indicates slightly faster CMEs in the southern hemisphere. This is consistent with the increase in the computed wind speed asymmetry shown in Table 4a following removal of the CMEs. The shocks themselves do not demonstrate a significant north-south asymmetry in the wind speed.

The average wind speeds listed in Tables 4a and 4b may be used to compute an average predicted winding angle $\Psi^{(P)}$ using (1) and associated parameters including $b = 0$. Tables 4a and 4b list these results; the error levels are computed from the uncertainties in the wind speed. The decreasing wind speeds listed in Table 4a as various disturbances are removed lead to slight increases in the predicted average winding angle. Likewise, the higher wind speeds contained within the disturbances lead to the smaller predicted winding angles listed in Table 4b. This comparison further demonstrates the role of CMEs and shocks in the apparent overwinding of the IMF: the higher wind speeds of the disturbed plasma should demonstrate the smallest winding angles, but Table 2 clearly demonstrates that the disturbances are overwound relative to theory.

### 3.4. IMF Component Statistics

An examination of the IMF components can lead us to conclude how the overwinding, and possibly the winding angle asymmetry, are accomplished and what source field is present closer to the Sun. The average field components are shown in Table 5 where the components are averaged across both hemispheres. This quantity does not address the IMF overwinding, but zero values for $B_R$ and $B_T$ would be consistent with the absence of a winding angle asymmetry. Both of these components are generally small and statistically insignificant in keeping with the winding angle asymmetry analysis. However, the $B_N$ component shows a statistically significant and negative average.

Examination of the distribution of values for the $B_N$ component offers some explanation for the above behavior. Figure 3 shows the distribution of $B_N$ values for the entire data set (top curve), undisturbed data as represented by combined subset 2 (middle curve), and the disturbance data subset as represented by all data not contained in combined subset 2 (bottom curve). The latter consists of CMEs extended to include their upstream shocks and non-CME shocks with the following 48 hours of data. The disturbance distribution shows a clear skewing to positive $B_N$, while the undisturbed data subset shows a less obvious skewing to negative values. Although not shown in the figure, the disturbance data subset has a greater number of observations with $|B_N| > 15$ than does the undisturbed data subset.

It is worth noting that the nonzero average N component behavior demonstrated in Table 5 and Figure 3 persists across the changing solar dipole and is not the result of a disproportional weighting of some process tied to the solar polarity since comparable values, including sign, exist for the undisturbed IMF both before and after the solar magnetic reversal of 1980. This analysis of ISEE 3 data agrees well with the same years of omnitape data analyzed by *Smith and Bieber* [1993] but points to the hitherto opposing relationship

between the average N component of CMEs and undisturbed data.

Since the IMF has opposite signs in the toward and away sectors and $\mathbf{B}^T = -\mathbf{B}^A$ in a symmetric hemisphere, $\frac{1}{2}\langle \mathbf{B}^T - \mathbf{B}^A \rangle$ is related to the average winding angle. Tables 6a and 6b show values for $\frac{1}{2}\langle \mathbf{B}^T - \mathbf{B}^A \rangle$ computed in the manner used throughout this paper. The results of Table 6a for the radial component show relatively little variation as the disturbances are removed, while the tangential component decreases by $3\sigma$. This suggests that CMEs and the regions downstream of shocks possess an enhanced tangential component relative to quiet periods. This is expected since CMEs represent the emergence of a closed-topology structure with fields markedly different from the *Parker* [1958] picture, while shock compression intensifies the component of the IMF perpendicular to the shock normal.

In spite of the significantly higher intensities for disturbances, as shown in Tables 3a and 3b, the computed average field components for disturbed data are remarkably small as shown in Table 6b, and the magnitude of the average magnetic field for disturbances is only $\sim$ 1 nT greater than for the undisturbed data. CMEs are reputed to display remarkably low fluctuation levels for the magnetic field. However, they do display large-scale structure with an internal field. This structure leads to a significant degree of cancellation in computing the average field components over a solar rotation and is the likely explanation for the reduced IMF components shown in Table 6b.

The average vector components shown in Tables 6a and 6b can be used to compute and average winding angle for the observations. These are listed in the final columns of Tables 6a and 6b. Removal of the disturbances leads to a reduction of the average winding angle by 1.8°, as expected if the disturbances are responsible for the measured overwinding of the IMF in spite of the high wind speed conditions of the disturbances. Comparison of the winding angles derived from the average field components in Table 6a with the predicted winding angles derived from the average wind speed and listed in Table 4a shows that there remain several degrees of overwinding in the undisturbed data that are not seen in Table 2. This is unique to the IMF component analysis and supports the suggestion by *Smith and Bieber* [1991] that periods of high field intensity in the omnitape data set possess greater winding angles than low-intensity intervals.

When the winding angle is derived from an average of the instantaneous unit vectors, thereby preventing the magnitude of the individual measurements from weighting the average, the resulting winding angle for all data in the ISEE 3 data set is 47.2° (3.5° smaller than the value listed in Table 6a). Likewise, the winding angle for combined subset 2 derived from the unit vector analysis is 46.0° (2.9° smaller than the full vector analysis). This provides further evidence that measurements of high field intensity display greater winding angles, even for observations of undisturbed plasma.

The concentration of the overwound field within the CMEs is made most graphic in Table 6b, which lists $\sim$ 10° greater winding angles for CMEs than for undisturbed data as listed in Table 6a. Non-CME shocks and their associated downstream plasma are only 3° overwound relative to the undisturbed plasma.

### 3.5. Source Fields

*Bieber and Rust* [1995, p. 911] make use

of the observation that "toroidal field components in [solar] active regions are almost all oriented in the same sense in each solar hemisphere (Hales's law)." The direction of the toroidal field reverses at solar maximum. The implication is that CMEs impart an extraneous tangential component to the IMF that is different within each heliospheric hemisphere over any given phase of the solar cycle. *Bieber and Rust* [1996] use this idea to describing the possibility of large magnetic toroids forming in the outer heliosphere that result from the merging of the CMEs and other disturbances.

Although the overwinding results may be interpreted in terms of an added radial component, it is most easily interpreted as an added tangential component which vanishes from the results of Table 6a as the disturbances are removed, allowing those observations to converge with the Parker theory to produce an average winding angle closer to the nominal 45° value predicted by the wind speed. We can use Table 6b to estimate the anomalous $|\langle B_T \rangle|$ contained within CMEs to be that value which returns the observed field within the disturbances to a 45° winding angle. For CMEs this is $2.1 \pm 0.5$ nT. This value represents an average over the entire volume of the CME as measured at Earth's orbit. The anomalous $B_T$ may not be added uniformly within the CME and almost certainly is not, while specific CME models may concentrate the anomalous $B_T$ within the leading edge of the disturbance [e.g., *Linker et al.*, 1990, Figure 3]. This additional T component of the IMF is added in such a way as to yield an average overwinding of the IMF in both hemispheres and is distinct from the anomalous $\langle B_T \rangle$ discussed by *Smith and Bieber* [1993] which is the same in both hemispheres and leads to an asymmetry in the winding angle. A detailed model describing the evolution of CMEs in the interplanetary medium is needed to relate the above value measured at 1 AU to the average azimuthal component of CME fields at the time of eruption. Such a model is beyond the scope of this paper.

## 4. Magnetic Flux

In a straightforward extension of the analysis techniques employed in this paper, it becomes possible to compare two recently proposed models for solar flux shedding in association with CMEs. First, *McComas et al.* [1992] compute estimates for the flux shedding of the Sun using the NSSDC omnitape and ISEE 3 data sets. They suggest, due to heightened flux levels during solar maximum, that CMEs are a principal carrier of the shed solar flux. Below we will isolate the CME source from other disturbances in a further test of this suggestion. Second, the overwinding result of earlier analyses is cited by *Bieber and Rust* [1995, 1996] as motivation for their model of disturbance-associated flux shedding and merging leading to the creation of magnetic toroids on a heliospheric scale. Bieber and Rust propose that a variety of solar ejecta, including CMEs, filament eruptions, and active region loop expansion are responsible for the ejection of flux into the solar wind. Having established that CMEs and interplanetary shocks are responsible for the apparent overwinding of the IMF, we now ask how much flux is carried by these disturbances.

### 4.1. Magnetic Flux Theory

Equations (1) to (4) of *McComas et al.* [1992] derive an expression for the convected solar magnetic flux, $\phi$, using GSE $(x, y, z)$ coordinates where $\hat{\mathbf{x}}$ is directed from the Earth to the Sun, $\hat{\mathbf{y}}$ lies within the Earth's orbital

plane and is directed in opposition to the Earth's orbital motion, and $\hat{\mathbf{z}} = \hat{\mathbf{x}} \times \hat{\mathbf{y}}$ completes the right-hand coordinate system. Correcting for a minor sign error between (3) and (4) of *McComas et al.* [1992] which propagates through (6) of that paper and rotating the expression to heliocentric $(R, T, N)$ coordinates, we may write

$$\phi = \int B_T V_R dt \tag{2}$$

under the identity $\hat{\mathbf{R}} = -\hat{\mathbf{x}}$ and the approximations $\hat{\mathbf{T}} \simeq -\hat{\mathbf{y}}$ and $\hat{\mathbf{N}} \simeq \hat{\mathbf{z}}$.

Since the flux integral of (2) must be zero if completely characterized by observations, *McComas et al.* [1992] introduced a quantity which represents the total flux of convected field lines encountered by the spacecraft, $\phi^*$. Adopting their definition and again applying the rotation to heliocentric coordinates under the above approximation, we get

$$\phi^* = \int |B_T| V_R dt. \tag{3}$$

The expression for $\phi^*$ can be extended by taking into account the flux in the $\hat{\mathbf{z}}$ or $\hat{\mathbf{N}}$ component. Equation (6) of *McComas et al.* [1992] defines

$$\phi^*_\perp = \int \sqrt{B_T^2 + B_N^2} V_R dt. \tag{4}$$

*McComas et al.* [1992] argue that the eruption of a CME drags new field lines, as measured by $\phi$, into interplanetary space, where they add to the interplanetary field. Unless the addition of field lines by CME eruption is balanced by reconnection somewhere, this process would lead to a steady increase in the magnitude of the IMF. On the basis of measurements of $\phi^*$ and $\phi^*_\perp$, McComas et al. conclude that such a buildup does not occur over timescales longer than a sunspot cycle. However, if a CME forms a pinched-off plasmoid that is no longer rooted in the subchromospheric plasma, then its contribution to the IMF is transitory. McComas et al. suggest that either CMEs reconnect into plasmoids with closed topology before reaching 1 AU or some other mechanism reduces buildup of the field. They postulate that reconnection of previously open field lines permits at least partial reduction in the IMF intensity.

*Bieber and Rust* [1995] adopt a slightly different expression for the measured ejection of solar magnetic flux. They define a coordinate system $(X, Y)$ oriented relative to the predicted spiral field as computed from (1) using the observed wind speed and a source surface at 5 solar radii. The $X$ coordinate is oriented along the predicted spiral field and away from the sun regardless of sector type. The $Y$ coordinate is at right angles to the IMF spiral, constrained to lie within the ecliptic plane, and always points outward from the Sun. Figure 4 demonstrates the relationship between the $(X, Y)$ coordinate system, the $(R, T)$ coordinates, and the spiral field of toward and away sectors. Equation (2) of *Bieber and Rust* [1995] then defines the toroidal solar magnetic flux passing the observer per unit time per unit of distance normal to the ecliptic plane to be

$$F_R = V_{SW} B_Y^{(P)} \cos(\Psi_P) \tag{5}$$

and the density of open magnetic flux by

$$B_R^{(P)} = B_X^{(P)} \cos(\Psi_P). \tag{6}$$

$B_R^{(P)}$ is denoted as $B_R$ by *Bieber and Rust* [1995] and is not to be confused with the radial component of the measured IMF. $B_X^{(P)}$ and $B_Y^{(P)}$ are the components of the measured IMF in the above spiral-oriented $(X, Y)$ coordinate system. Bieber and Rust then apply (5) and (6) so that toward and away sector measurements are subtracted, as described later, and the results are integrated over time

in a manner generally consistent with (2) – (4).

From (2) to (6) we can compute estimates of the average solar magnetic flux density. We get

$$\delta\phi = B_T V_{sw} \quad (7)$$

$$\delta\phi^* = |B_T| V_{sw} \quad (8)$$

$$\delta\phi^*_\perp = \sqrt{B_T^2 + B_N^2}\, V_{sw} \quad (9)$$

$$\delta\phi_{\rm toroid} = V_{sw} B_Y^{(P)} \cos(\Psi_P) \quad (10)$$

$$\delta\phi_{\rm open} = B_X^{(P)} \cos(\Psi_P). \quad (11)$$

Equations (7) through (10) represent flux rate densities, while (11) is the local flux density of the spiral-aligned component of the field. Evaluation of the total flux rates from (7) through (10) requires an over a closed surface encompassing the Sun, while the computations of the total flux require an additional integration over time. Evaluation of the total flux of open field lines from (11) simply requires an integration over the closed surface encompassing the Sun. We choose to compute average flux rate densities which we prorate according to data coverage to estimate the average yearly flux over the lifetime of the ISEE 3 mission at $L_1$.

### 4.2. Magnetic Flux Observations

We have evaluated (7) through (11) using the ISEE 3 data set in the same manner as the statistics of the preceeding section were computed. The results are consistent with the earlier tabulations of the IMF and solar wind statistics. We compute averages of (7) through (11) over individual solar rotations while selectively removing subsets of the total data set such as CMEs and shocks. We then combine the individual solar rotation values as before according to whether we are seeking heliospheric averages, the north-south asymmetry, or toward-away differences which are key to the results of this section. This yields estimates of the magnetic field flux as defined by *McComas et al.* [1992] and *Bieber and Rust* [1995] and allows us to assign the relative importance of CMEs, shocks, and the undisturbed solar wind in the computed net solar magnetic flux.

Table 7 lists the results of averaging the flux expressions over the two sector types. The average of the sign-dependent quantities $\delta\phi$, $\delta\phi_{\rm open}$, and $\delta\phi_{\rm toroid}$ are small and differ from zero by only $1\sigma$. These results are not shown but are consistent with the overall symmetry of the flux ejection process. There is a statistically significant reduction in the average convected field lines $\langle\delta\phi^*\rangle$ and $\langle\delta\phi^*_\perp\rangle$ as disturbances are removed, which is consistent with there being higher values of field intensity and wind speed within disturbances as shown in Tables 3a through 4b.

We can compare the measured values of $\langle\delta\phi^*\rangle$ given in Table 7 with the results of *McComas et al.* [1992] by multiplying $\langle\delta\phi^*\rangle$ by one solar rotation, in which case the average flux of field lines integrated over 27 days is $(4.6\pm0.1)\times10^3$ Wb $\cdot$ m$^{-1}$ at Earth orbit. This is 24% larger than the value stated in Figure 4 of their paper, but this can be explained by the temporal trend in the McComas et al. data and by the different time interval used in the present study. If we compare the first two rows of Table 7 and prorate the results according to coverage, we find that the flux density within CMEs as measured by $\langle\delta\phi^*\rangle$ is 52% greater than in the remainder of the solar wind. Similar enhancements exist downstream of the CME-associated and non-CME shocks.

The averages of the five flux expressions may be viewed as either averages across the two hemispheres or as averages across the two sector types. We have looked for a persistent

north-south asymmetry in these five quantities but have not found a result with greater than a $1\sigma$ significance. This is consistent with a high degree of north-south symmetry for CMEs and shock sources. These results are not shown.

*Bieber and Rust* [1995] followed the suggestions of *Parker* [1984, 1987] wherein magnetic buoyancy carries flux to the solar surface for ejection into the solar wind plasma at what may be widely dispersed bipolar regions. Since this is a local process acting within a global structure, each solar hemisphere must act to eject its flux independently of the other. The average rate of flux ejection can then be computed if we construct sector-differenced averages in the manner prescribed by *Bieber and Rust* [1995]. Following their approach, we add away sector values of $\delta\phi_{\rm open}$ to negative toward sector values of the same to construct a sector-differenced quantity which we call $\Delta^{AT}(\delta\phi_{\rm open})$ and average to estimate the average amount of open flux. Also following the Bieber and Rust approach, we add toward and negative away values of $\delta\phi_{\rm toroid}$, which we denote as $\Delta^{TA}(\delta\phi_{\rm toroid})$, to estimate the average rate of toroidal flux ejection under the assumption that each hemisphere ejects toroidal flux of a particular sign depending upon the phase of the solar dipole. We do the same with measurements of $\delta\phi$ to construct estimates of magnetic field line ejection following the *McComas et al.* [1992] formalism. Table 8a lists the results of this analysis.

Table 8a shows first of all that there is more than an order of magnitude difference between the estimate for $\frac{1}{2}\langle\Delta^{TA}(\delta\phi)\rangle$ derived from the *McComas et al.* [1992] expression for the convection of flux in the solar wind and the estimate for $\frac{1}{2}\langle\Delta^{TA}(\delta\phi_{\rm toroid})\rangle$ derived from the *Bieber and Rust* [1995] expression. It appears that about 8% of the total convected flux is toroidal during solar maximum.

Table 8a also shows that the flux density of toroidal field lines is largely confined to disturbances, both CMEs and shocked plasma. Removal of the CMEs alone (as represented by CME subset 1) reduces the average flux of newly injected field lines derived from $\langle\delta\phi\rangle$ by $56. \pm 64.$ nT $\cdot$ km $\cdot$ s$^{-1}$. This is about twice the $\langle\delta\phi_{\rm toroid}\rangle$ result, which is $27. \pm 28.$ nT $\cdot$ km $\cdot$ s$^{-1}$.

Removal of the shocked plasma between the CMEs and the upstream shocks in addition to the CMEs (as represented by CME subset 2) reduces the computed average flux of field lines by yet as much again to yield a net change in $\frac{1}{2}\langle\Delta^{TA}(\delta\phi)\rangle$ relative to the whole data set of $106. \pm 64.$ nT $\cdot$ km $\cdot$ s$^{-1}$. Likewise, the change in the flux density of toroidal field lines at $53. \pm 29.$ nT $\cdot$ km $\cdot$ s$^{-1}$ is nearly double that of removing the CMEs alone. The field lines between the CME and the shock are widely regarded to be open field lines, although they may have undergone subsequent reconnection within the solar wind [*McComas et al.*, 1992] and therefore would not be expected to contribute to the flux of newly ejected field lines. The removal of the potentially disturbed plasma downstream of the CME, as represented by CME subset 3, does little to change the result.

The reason why interplanetary shocks provide a significant error source to the computed flux rate of toroidal field lines when the region immediately behind the shock is generally expected to be composed of open field lines can be inferred from Tables 2 through 6b. The statistics for toroidal flux ejection as determined by $\langle\Delta^{TA}(\delta\phi_{\rm toroid})\rangle$ track the statistics for field line overwinding as given by Table 2 so that as shocked plasma is removed from the data set, the computed flux of toroidal field lines decreases even though the field lines are

generally regarded as open. The statistics for $\langle \Delta^{TA}(\delta\phi) \rangle$ more nearly tracks with the wind speed and field strength, but is also enhanced by overwinding.

We can reproduce the conclusions of *Bieber and Rust* [1995] for the total net yearly-averaged flux of toroidal magnetic field lines by multiplying the computed average rate $\frac{1}{2}\langle \Delta^{TA}(\delta\phi_{\rm toroid}) \rangle$ for the entire data set listed in the top row of Table 8a by the number of seconds in a year and the appropriate geometrical factor $\pi R$ (a factor of 2 larger than that used by Bieber and Rust owing to our averages in Table 8a). $R$ is the spacecraft-to-Sun distance, which is $1.5 \times 10^8$ km. For estimates of the total flux of open field lines the factor is $4\pi R^2$, and no integration over time is required as a multiplicative factor for $\frac{1}{2}\langle \Delta^{AT}(\delta\phi_{open}) \rangle$. *Hundhausen* [1993] reports that CMEs are seen at high latitudes and evenly distributed over latitudes up to 60° during years of solar maximum so we will integrate our computed averages over the full sphere as do Bieber and Rust. The resulting estimate for the net total flux of toroidal field lines is $(2.16 \pm 0.03) \times 10^{23}$ Mx $\cdot$ yr$^{-1}$, which is in good agreement with the conclusions of Bieber and Rust for the same years. For open field lines, our analysis yields an average net flux of $(1.04 \pm 0.02) \times 10^{23}$ Mx, which also agrees well with the Bieber and Rust result and with the average radial component of the IMF as listed in Table 6a.

A relatively small flux of toroidal field lines persists in the data set following the removal of CMEs and shock disturbances. If we consider that combined subset 2 retains 78% of all data within the total data set, then the computed net yearly flux of toroidal field lines by undisturbed plasma is $(4.5 \pm 3.6) \times 10^{22}$ Mx $\cdot$ yr$^{-1}$, which is 21% of the total flux of toroidal field lines as computed for all data.

It is likely that our analysis using both the *McComas et al.* [1992] and *Bieber and Rust* [1995] formalisms overstates the presence of toroidal field lines. The McComas et al. treatment makes no distinction between open and toroidal field lines, and our assignment of residual fields in column 1 of Table 8a to toroidal structures neglects contributions from open fields. The Bieber and Rust formalism identifies as toroidal any region with non-Parker fields. This treatment neglects, for example, non-Parker open fields caused by stream interaction regions. We have argued above that this is the case when shocked plasma is considered and it may be true generally. Alternatively, there may be additional sources of toroidal field line flux such as field line reconnection ahead of CMEs [*McComas et al.*, 1995] or the ejection of flux by filament eruptions and active region loop expansion as suggested by *Bieber and Rust* [1995].

We can use the second column in Table 8a to estimate the net flux of toroidal field lines due to CMEs. CME subset 1 represents 92% of the data set, which results in an estimate of $(1.62 \pm 0.03) \times 10^{23}$ Mx $\cdot$ yr$^{-1}$ of flux for toroidal magnetic field lines from this subset. This leaves 25% of the original value, or approximately $0.54 \times 10^{23}$ Mx $\cdot$ yr$^{-1}$ of flux, to be carried by CMEs.

We can apply the expressions for flux ejection to the CME and shock disturbances directly. Table 8b shows the results of this analysis where again sector-differenced averages are tabulated. These quantities are in good agreement with what can be inferred from Table 8a. As anticipated, the average flux densities contained within the disturbed plasma are greater than the averages shown in Table 8a since both the wind speed and the field intensity are greater within the disturbances and the fields are overwound. Also as antic-

ipated, the average magnetic flux density for shocked plasma is less than values computed for CMEs. The plasma between CMEs and their associated upstream shocks adds somewhat to the CME-associated flux.

From the values listed in Table 8b and the recognition that CMEs constitute only 8% of the data, we compute a yearly ejection rate of toroidal solar flux within CMEs to be

$$\langle \phi_{\rm toroid} \rangle^{\rm CMEs} = (6.07 \pm 0.13) \times 10^{22} \ {\rm Mx \cdot yr^{-1}}. \quad (12)$$

*Vainshtein and Rosner* [1991] estimate that the Sun must shed $10^{23}$ Mx every 6 years in order to maintain the solar dynamo without an unlimited buildup of the field. On average this analysis obtains as much flux shedding by CMEs every two years during the period from 1979 through 1982 as Vainshtein and Rosner require in a 6-year period. This somewhat heightened rate may derive from the assumption in this paper that the measured rate at Earth's orbit can be taken as representative of high-latitude fields and suggests that flux shedding at high latitudes may be significantly reduced relative to near-ecliptic observations.

The yearly average flux of open field lines within CMEs at Earth's orbit as computed by this formalism is

$$\langle \phi_{\rm open} \rangle^{\rm CMEs} = (9.17 \pm 0.57) \times 10^{21} \ {\rm Mx}. \quad (13)$$

## 5. Conclusions

We conclude that CMEs, their upstream shocks, and non-CME shocks account for the apparent overwinding of the IMF reported in earlier investigations. The processing of the interplanetary plasma by these disturbances lies outside the traditional *Parker* [1958] description for the winding of the IMF, and so it is not unexpected that these transient disturbances would skew the statistics.

This fact is made more interesting by the realization that many CMEs and the non-CME shocks represent high-speed plasma. In open-field regions, one expects the fields to be less tightly wound when the solar wind speed is higher, but CMEs possess a closed-field topology and the average winding angle is greater than in open-field measurements in spite of the higher average wind speed for CMEs. Shocked plasma tends to have greater azimuthal fields as well due to compression across the shock and therefore possesses greater winding angles on average than the Parker theory would predict based upon the local wind speed.

It is also interesting that these disturbances do not appear to account for the observed north-south asymmetry of the IMF winding angle. Since CME coverage appears to be evenly distributed between the northern and southern hemispheres, the processes which affect the overwinding do not introduce an additional asymmetry component. A persistent north-south winding angle asymmetry remains an apparent attribute of the undisturbed solar wind.

*Smith and Bieber* [1991] suggest that the apparent overwinding of the IMF might result from a small azimuthal field at the source region. They also postulate how such a field might arise as a remnant of fields from deeper within the chromosphere. This seed field would then contribute a small but persistent winding of the IMF over the solar poles in contrast to the straight field lines predicted by *Parker* [1958]. To the extent that such a seed field would produce an overwinding at all latitudes, there now appears to be no motivation for this small azimuthal source field except to the extent that CMEs are expected to contain nonradial fields at the source surface. It remains possible that an azimuthal seed field

exists for sources of open field lines, but this field would need to produce an overwinding in one hemisphere and an underwinding in the other, so that no net overwinding was present but the winding angle asymmetry remained.

We have also examined the flux of open and toroidal magnetic field lines as defined by previous authors and the relative density of these quantities within CMEs and the disturbances downstream of shocks. We find that CMEs contain only $\sim$ 25% of the total computed flux of "toroidal field" lines observed at Earth orbit, as measured by previously published formulations. The computed density of toroidal field line flux in the disturbed plasma downstream of interplanetary shocks is approximately half as great as for CMEs. No significant north-south asymmetry of magnetic flux is observed.

**Acknowledgments.** We wish to thank Ed Smith and Jack Gosling who contributed the data used in this study. We thank Jack Gosling and Dave McComas for their contributions to the CME and shock catalog. We acknowledge helpful discussions with John Bieber and David Rust. We also thank both referees who made helpful comments on the paper. Work at the Bartol Research Institute was supported by NASA grant NAGW-3033 with partial support from the NASA Delaware Space Grant College NGT 40023. Work at Los Alamos was performed under the auspices of the U.S. Department of Energy.

The Editor thanks two referees for their assistance in evaluating this paper.

## References

Bieber, J. W., North-south asymmetry of the interplanetary magnetic field spiral, *J. Geophys. Res.*, *93*, 5903-5907, 1988.

Bieber, J. W., and D. M. Rust, The escape of magnetic flux from the Sun, *Astrophys. J.*, *453*, 911-918, 1995.

Bieber, J. W., and D. M. Rust, The escape of magnetic toroids from the Sun, in *Solar Wind 8*, Am. Inst. of Phys., New York, in press, 1996.

Forbush, S. E., S. P. Duggal, M. A. Pomerantz, and C. H. Tsao, Random fluctuations, persistence, and quasi-persist-ence in geophysical and cosmical periodicities: A sequel, *Rev. Geophys.*, *20*, 971-976, 1982.

Forbush, S. E., M. A. Pomerantz, S. P. Duggal, and C. H. Tsao, Statistical considerations in the analysis of solar oscillation data by the superposed epoch method, *Sol. Phys.*, *82*, 113-122, 1983.

Gazis, P. R., Limits on deceleration and asymmetry of solar wind speed, *Geophys. Res. Lett.*, *22*, 2441-2444, 1995.

Goldstein, B. E., M. Neugebauer, J. L. Phillips, S. J. Bame, J. T. Gosling, D. J. McComas, Y.-M. Wang, N. R. Sheeley Jr., and S. T. Suess, Ulysses plasma parameters: Latitudinal, radial, and temporal variations, *Astron. Astrophys.*, in press, 1996.

Gosling, J. T., Coronal mass ejections and magnetic flux ropes in interplanetary space, in *Physics of Magnetic Flux Ropes*, Geophys. Monogr. Ser., vol. 58, edited by C. T. Russell, E. R. Priest, and L. C. Lee, pp. 343-364, AGU, Washington, D.C., 1990.

Gosling, J. T., E. Hilder, R. M. MacQueen, R. H. Munro, A. I. Poland, and C. L. Ross, The speeds of coronal mass ejection events, *Sol. Phys.*, *48*, 389-397, 1976.

Gosling, J. T., D. N. Baker, S. J. Bame, W. C. Feldman, and R. D. Zwickl, Bidirectional solar wind electron heat flux events, *J. Geophys. Res.*, *92*, 8519-8535, 1987.

Hundhausen, A. J., Sizes and locations of coronal

mass ejections: SMM observations from 1980 and 1984-1989, *J. Geophys. Res.*, *98*, 13,177-13,200, 1993.

Linker, J. A., G. van Hoven, and D. D. Schnack, Effects of the driving mechanism in MHD simulations of coronal mass ejections, in *Physics of Magnetic Flux Ropes*, Geophys. Monogr. Ser., vol. 58, edited by C. T. Russell, E. R. Priest, and L. C. Lee, pp. 379-384, AGU, Washington, D.C., 1990.

McComas, D. J., J. T. Gosling, S. J. Bame, E. J. Smith, and H. V. Cane, A test of magnetic field line draping induced $B_z$ perturbations ahead of fast coronal mass ejecta, *J. Geophys. Res.*, *94*, 1465-1471, 1989.

McComas, D. J., J. T. Gosling, and J. L. Phillips, Interplanetary magnetic flux: Measurement and balance, *J. Geophys. Res.*, *97*, 171-177, 1992.

McComas, D. J., J. T. Gosling, C. M. Hammond, M. B. Moldwin, J. L. Phillips, and R. J. Forsyth, Reconnection on open field lines ahead of coronal mass ejections, *Space Sci. Rev.*, *72*, 129-132, 1995.

Parker, E. N., Dynamics of the interplanetary gas and magnetic fields, *Astrophys. J.*, *128*, 664-676, 1958.

Parker, E. N., *Interplanetary Dynamical Processes*, Wiley-Interscience, New York, 1963.

Parker, E. N., Magnetic buoyancy and the escape of magnetic fields from stars, *Astrophys. J.*, *281*, 839-845, 1984.

Parker, E. N., The dynamo dilemma, *Sol. Phys.*, *110*, 11-21, 1987.

Phillips, J. L., J. T. Gosling, D. J. McComas, S. J. Bame, and W. C. Feldman, Quantitative analysis of bidirectional electron fluxes within coronal mass ejections at 1 AU, in *Proceedings of the 1$^{st}$ SOLTIP Symposium*, edited by S. Fischer and M. Vandas, pp. 165-170, Czechoslovak Acad. of Sci., Prague, Czech Republic, 1992.

Phillips, J. L., J. T. Gosling, and D. J. McComas, Coronal mass ejections and geomagnetic storms: Season variations, in *Solar-Terrestrial Predictions IV*, edited by J. Hruska, M. A. Shea, D. F. Smart, and G. Heckman, pp. 242-250, Natl. Oceanic and Atmos. Admin., Boulder, Colo., 1993.

Richardson, J. D., K. I. Paularena, A. J. Lazarus, and J. W. Belcher, Evidence of a solar wind slowdown in the outer heliosphere?, *Geophys. Res. Lett.*, *22*, 1469-1472, 1995.

Rosenberg, R. L., and P. J. Coleman Jr., Heliographic latitude dependence of the dominant polarity of the interplanetary magnetic field, *J. Geophys. Res.*, *74*, 5611-5622, 1969.

Sabbah, I., Persistent larger IMF spiral north of the heliospheric current sheet than south of it, *Conf. Pap. Int. Cosmic Ray Conf. XXIV*, *4*, 513-516, 1995.

Sabbah, I., Persistent north-south asymmetry of the daily interplanetary magnetic field spiral, *J. Geophys. Res.*, *101*, 2485-2491, 1996.

Smith, C. W., and J. W. Bieber, Solar cycle variation of the interplanetary magnetic field spiral, *Astrophys. J.*, *370*, 435-441, 1991.

Smith, C. W., and J. W. Bieber, Observational study of the IMF spiral north and south of the current sheet, in *Solar Wind Seven*, edited by E. Marsch and R. Schwenn, pp. 273-276, Pergamon, Tarrytown, N.Y., 1992.

Smith, C. W., and J. W. Bieber, Multiple spacecraft survey of the north-south asymmetry of the interplanetary magnetic field, *J. Geophys. Res.*, *98*, 9401-9415, 1993.

Smith, C. W., and J. W. Bieber, Comment on "The underlying magnetic field direction in Ulysses observations of the southern polar heliosphere" by Forsyth et al., *Geophysical Research Letters*, in press, 1996.

Smith, C. W., and J. L. Phillips, The role of CMEs and interplanetary shocks in IMF winding angle statistics, in *Solar Wind 8*, Am. Inst. of Phys., New York, in press, 1996.

Vainshtein, S. I., and R. Rosner, On turbulent diffusion of magnetic fields and the loss of magnetic flux from stars, *Astrophys. J.*, *376*, 199-203, 1991.

Weber, E. J., and L. Davis Jr., The angular mo-

mentum of the solar wind, *Astrophys. J.*, *148*, 217-227, 1967.

Weber, E. J., and L. Davis Jr., The effect of viscosity and anisotropy in the pressure on the azimuthal motion of the solar wind, *J. Geophys. Res.*, *75*, 2419-2428, 1970.

J.L. Phillips, Los Alamos National Laboratory, Los Alamos, NM 87545. (e-mail: jlphillips@lanl.gov)

C.W. Smith, Bartol Research Institute, University of Delaware, Newark, DE 19716. (e-mail: chuck@bartol.udel.edu)

March 18, 1996; revised August 6, 1996; accepted August 29, 1996.

This preprint was prepared with AGU's LaTeX macros v4. File CMEJGR formatted November 13, 1996.

**Table 1.** ISEE 3 Subset Definitions

| ISEE 3 Subset | Definition |
|---|---|
| All data in data set | no data removed |
| CME subset 1 | CMEs removed |
| CME subset 2 | CMEs to upstream shock removed |
| CME subset 3 | CMEs to upstream shock removed along with trailing 24 hours |
| Shock subset 1 | non-CME shocks with trailing 24 hours removed |
| Shock subset 2 | non-CME shocks with trailing 48 hours removed |
| Combined subset 1 | CMEs to upstream shock plus non-CME shocks with trailing 24 hours removed |
| Combined subset 2 | CMEs to upstream shock plus non-CME shocks with trailing 48 hours removed |

[a]Year 1980 is always excluded from analysis.

**Table 2.** Winding Angle Statistics

| ISEE 3 Subset | Overwinding | Asymmetry |
|---|---|---|
| All data in data set | $1.4° \pm 0.6°$ | $1.5° \pm 1.5°$ |
| CME subset 1 | $0.8° \pm 0.5°$ | $0.9° \pm 1.5°$ |
| CME subset 2 | $0.5° \pm 0.6°$ | $1.0° \pm 1.5°$ |
| CME subset 3 | $0.5° \pm 0.5°$ | $0.6° \pm 1.6°$ |
| Shock subset 1 | $1.1° \pm 0.6°$ | $1.5° \pm 1.5°$ |
| Shock subset 2 | $1.1° \pm 0.6°$ | $1.7° \pm 1.4°$ |
| Combined subset 1 | $0.1° \pm 0.6°$ | $0.8° \pm 1.5°$ |
| Combined subset 2 | $0.0° \pm 0.6°$ | $1.3° \pm 1.4°$ |

[a]Overwinding and asymmetry angles are in degrees.

**Table 3a.** Field Magnitude Statistics

| ISEE 3 Subset | $\frac{1}{2}\langle\|B^N\| + \|B^S\|\rangle$ | $\frac{1}{2}\langle\|B^N\| - \|B^S\|\rangle$ |
|---|---|---|
| All data in data set | $7.77 \pm 0.21$ | $-0.13 \pm 0.13$ |
| CME subset 1 | $7.56 \pm 0.20$ | $-0.17 \pm 0.13$ |
| CME subset 2 | $7.38 \pm 0.20$ | $-0.14 \pm 0.13$ |
| CME subset 3 | $7.28 \pm 0.23$ | $-0.21 \pm 0.16$ |
| Shock subset 1 | $7.57 \pm 0.21$ | $-0.15 \pm 0.12$ |
| Shock subset 2 | $7.54 \pm 0.22$ | $-0.19 \pm 0.13$ |
| Combined subset 1 | $7.13 \pm 0.20$ | $-0.17 \pm 0.12$ |
| Combined subset 2 | $7.12 \pm 0.21$ | $-0.21 \pm 0.13$ |

[a]Field values are in nanoTesla.

**Table 3b.** Field Magnitude Statistics (Disturbances)

| ISEE 3 Subset | $\frac{1}{2}\langle\|B^N\| + \|B^S\|\rangle$ | $\frac{1}{2}\langle\|B^N\| - \|B^S\|\rangle$ |
|---|---|---|
| CMEs only | $10.3 \pm 0.4$ | $0.4 \pm 0.2$ |
| CMEs to shock | $11.4 \pm 0.5$ | $0.3 \pm 0.3$ |
| Non-CME shocks + 24 hours | $10.2 \pm 0.4$ | $0.2 \pm 0.3$ |

[a]Field values are in nanoTesla.

**Table 4a.** Wind Speed Statistics

| ISEE 3 Subset | $\frac{1}{2}\langle V_{sw}^N + V_{sw}^S\rangle$, km · s$^{-1}$ | $\frac{1}{2}\langle V_{sw}^N - V_{sw}^S\rangle$, km · s$^{-1}$ | $\Psi^{(P)}$, deg |
|---|---|---|---|
| All data in data set | $427.0 \pm 6.4$ | $3.7 \pm 4.1$ | $45.0° \pm 0.4°$ |
| CME subset 1 | $425.7 \pm 6.5$ | $4.4 \pm 4.2$ | $45.1° \pm 0.4°$ |
| CME subset 2 | $423.6 \pm 6.5$ | $4.4 \pm 4.2$ | $45.2° \pm 0.5°$ |
| CME subset 3 | $421.2 \pm 6.8$ | $5.2 \pm 4.6$ | $45.4° \pm 0.5°$ |
| Shock subset 1 | $426.1 \pm 6.3$ | $3.4 \pm 4.1$ | $45.1° \pm 0.3°$ |
| Shock subset 2 | $424.8 \pm 6.5$ | $3.9 \pm 4.3$ | $45.1° \pm 0.4°$ |
| Combined subset 1 | $422.1 \pm 6.5$ | $4.0 \pm 4.2$ | $45.3° \pm 0.5°$ |
| Combined subset 2 | $421.0 \pm 6.7$ | $4.6 \pm 4.4$ | $45.4° \pm 0.5°$ |

**Table 4b.** Wind Speed Statistics (Disturbances)

| ISEE 3 Subset | $\frac{1}{2}\langle V_{sw}^N + V_{sw}^S\rangle$, km · s$^{-1}$ | $\frac{1}{2}\langle V_{sw}^N - V_{sw}^S\rangle$, km · s$^{-1}$ | $\Psi^{(P)}$, deg |
|---|---|---|---|
| CMEs only | $443.2 \pm 11.1$ | $-7.0 \pm 5.2$ | $43.9° \pm 0.8°$ |
| CMEs to shock | $455.1 \pm 11.8$ | $-3.0 \pm 5.3$ | $43.2° \pm 0.7°$ |
| Non-CME shocks + 24 hours | $465.5 \pm 14.3$ | $-3.2 \pm 7.5$ | $43.1° \pm 1.0°$ |

**Table 5.** Field Component Averages

| ISEE 3 Subset | $\frac{1}{2}\langle B_R^N + B_R^S \rangle$, nT | $\frac{1}{2}\langle B_T^N + B_T^S \rangle$, nT | $\frac{1}{2}\langle B_N^N + B_N^S \rangle$, nT |
|---|---|---|---|
| All data in data set | $-0.07 \pm 0.10$ | $-0.08 \pm 0.10$ | $-0.19 \pm 0.10$ |
| CME subset 1 | $-0.12 \pm 0.11$ | $-0.10 \pm 0.10$ | $-0.23 \pm 0.11$ |
| CME subset 2 | $-0.11 \pm 0.12$ | $-0.11 \pm 0.10$ | $-0.24 \pm 0.11$ |
| CME subset 3 | $-0.14 \pm 0.15$ | $-0.11 \pm 0.12$ | $-0.18 \pm 0.12$ |
| Shock subset 1 | $-0.06 \pm 0.10$ | $-0.10 \pm 0.09$ | $-0.21 \pm 0.10$ |
| Shock subset 2 | $-0.09 \pm 0.10$ | $-0.10 \pm 0.10$ | $-0.23 \pm 0.11$ |
| Combined subset 1 | $-0.10 \pm 0.12$ | $-0.13 \pm 0.09$ | $-0.25 \pm 0.11$ |
| Combined subset 2 | $-0.12 \pm 0.12$ | $-0.12 \pm 0.10$ | $-0.28 \pm 0.11$ |

**Table 6a.** Field Component Differences

| ISEE 3 Subset | $\frac{1}{2}\langle B_R^T - B_R^A \rangle$, nT | $\frac{1}{2}\langle B_T^T - B_T^A \rangle$, nT | $\frac{1}{2}\langle B_N^T - B_N^A \rangle$, nT | $\langle \Psi \rangle$, deg |
|---|---|---|---|---|
| All data in data set | $-3.31 \pm 0.09$ | $4.05 \pm 0.11$ | $0.16 \pm 0.09$ | $50.7° \pm 1.6°$ |
| CME subset 1 | $-3.30 \pm 0.09$ | $3.94 \pm 0.11$ | $0.13 \pm 0.09$ | $50.1° \pm 1.5°$ |
| CME subset 2 | $-3.28 \pm 0.09$ | $3.86 \pm 0.11$ | $0.10 \pm 0.09$ | $49.6° \pm 1.6°$ |
| CME subset 3 | $-3.25 \pm 0.10$ | $3.86 \pm 0.13$ | $0.16 \pm 0.09$ | $49.9° \pm 1.8°$ |
| Shock subset 1 | $-3.27 \pm 0.09$ | $3.93 \pm 0.11$ | $0.12 \pm 0.09$ | $50.2° \pm 1.6°$ |
| Shock subset 2 | $-3.28 \pm 0.09$ | $3.93 \pm 0.12$ | $0.15 \pm 0.09$ | $50.2° \pm 1.6°$ |
| Combined subset 1 | $-3.23 \pm 0.09$ | $3.71 \pm 0.12$ | $0.06 \pm 0.09$ | $49.0° \pm 1.7°$ |
| Combined subset 2 | $-3.24 \pm 0.09$ | $3.71 \pm 0.13$ | $0.08 \pm 0.09$ | $48.9° \pm 1.7°$ |

**Table 6b.** Field Component Differences (Disturbances)

| ISEE 3 Subset | $\frac{1}{2}\langle B_R^T - B_R^A \rangle$, nT | $\frac{1}{2}\langle B_T^T - B_T^A \rangle$, nT | $\frac{1}{2}\langle B_N^T - B_N^A \rangle$, nT | $\langle \Psi \rangle$, deg |
|---|---|---|---|---|
| CMEs only | $-2.94 \pm 0.33$ | $5.02 \pm 0.35$ | $0.48 \pm 0.38$ | $59.6° \pm 4.5°$ |
| CMEs to shock | $-3.21 \pm 0.29$ | $5.54 \pm 0.35$ | $0.52 \pm 0.43$ | $59.9° \pm 3.7°$ |
| Non-CME shocks + 24 hrs | $-3.75 \pm 0.31$ | $4.79 \pm 0.41$ | $0.80 \pm 0.28$ | $51.9° \pm 4.6°$ |

**Table 7.** Average Flux Statistics

| ISEE 3 Subset | $\langle \delta\phi^* \rangle$ [a] | $\langle \delta\phi^*_\perp \rangle$ [a] |
|---|---|---|
| All data in data set | $1946. \pm 55.$ | $2618. \pm 80.$ |
| CME subset 1 | $1868. \pm 51.$ | $2514. \pm 72.$ |
| CME subset 2 | $1802. \pm 49.$ | $2408. \pm 68.$ |
| CME subset 3 | $1781. \pm 55.$ | $2349. \pm 73.$ |
| Shock subset 1 | $1881. \pm 57.$ | $2528. \pm 82.$ |
| Shock subset 2 | $1871. \pm 60.$ | $2503. \pm 85.$ |
| Combined subset 1 | $1717. \pm 50.$ | $2291. \pm 68.$ |
| Combined subset 2 | $1708. \pm 52.$ | $2273. \pm 71.$ |

[a] *McComas et al.* [1992] formalism.

[b] Flux values are in $\mathrm{nT \cdot km \cdot s^{-1}}$.

**Table 8a.** Sector Flux Asymmetry Statistics

| ISEE 3 Subset | $\frac{1}{2}\langle \Delta^{TA}(\delta\phi) \rangle$, [a] $\mathrm{nT \cdot km \cdot s^{-1}}$ | $\frac{1}{2}\langle \Delta^{TA}(\delta\phi_{\mathrm{toroid}}) \rangle$, [b] $\mathrm{nT \cdot km \cdot s^{-1}}$ | $\frac{1}{2}\langle \Delta^{AT}(\delta\phi_{\mathrm{open}}) \rangle$, [b] nT |
|---|---|---|---|
| All data in data set | $1710. \pm 46.$ | $145. \pm 19.$ | $3.67 \pm 0.08$ |
| CME subset 1 | $1654. \pm 45.$ | $118. \pm 20.$ | $3.60 \pm 0.08$ |
| CME subset 2 | $1604. \pm 44.$ | $92. \pm 22.$ | $3.55 \pm 0.08$ |
| CME subset 3 | $1600. \pm 51.$ | $97. \pm 26.$ | $3.52 \pm 0.08$ |
| Shock subset 1 | $1654. \pm 49.$ | $126. \pm 21.$ | $3.58 \pm 0.09$ |
| Shock subset 2 | $1651. \pm 52.$ | $123. \pm 22.$ | $3.58 \pm 0.09$ |
| Combined subset 1 | $1533. \pm 48.$ | $64. \pm 24.$ | $3.44 \pm 0.08$ |
| Combined subset 2 | $1528. \pm 51.$ | $39. \pm 31.$ | $3.37 \pm 0.09$ |

[a] *McComas et al.* [1992] formalism.

[b] *Bieber and Rust* [1995] formalism.

**Table 8b.** Sector Flux Asymmetry Statistics (Disturbances)

| ISEE 3 Subset | $\frac{1}{2}\langle \Delta^{TA}(\delta\phi) \rangle$, [a] $\mathrm{nT \cdot km \cdot s^{-1}}$ | $\frac{1}{2}\langle \Delta^{TA}(\delta\phi_{\mathrm{toroid}}) \rangle$, [b] $\mathrm{nT \cdot km \cdot s^{-1}}$ | $\frac{1}{2}\langle \Delta^{AT}(\delta\phi_{\mathrm{open}}) \rangle$, [b] nT |
|---|---|---|---|
| CMEs only | $2239. \pm 181.$ | $510. \pm 121.$ | $4.05 \pm 0.25$ |
| CMEs to shock | $2542. \pm 168.$ | $643. \pm 102.$ | $4.45 \pm 0.26$ |
| Non-CME shocks + 24 hours | $2098. \pm 180.$ | $222. \pm 113.$ | $4.40 \pm 0.25$ |

[a] *McComas et al.* [1992] formalism.

[b] *Bieber and Rust* [1995] formalism.

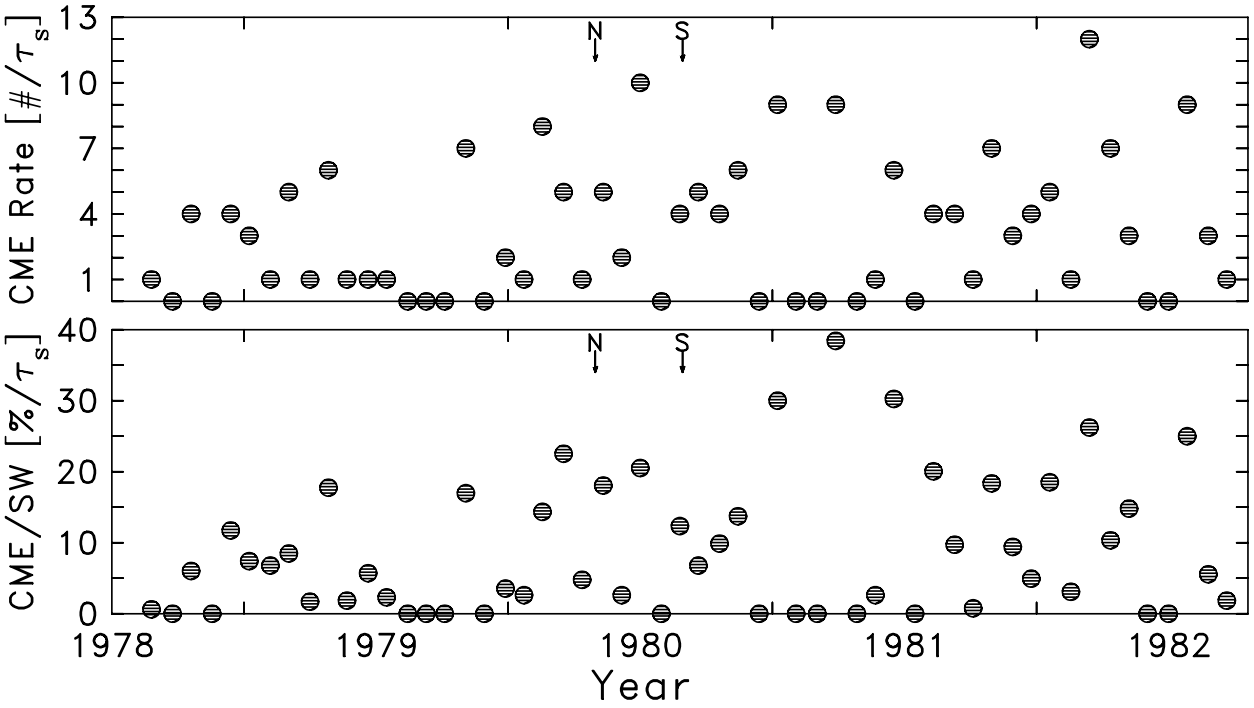


**Figure 1.** (Top) Number of CMEs per solar rotation as recorded by the ISEE 3 spacecraft. Times of north (N) and south (S) solar magnetic pole reversals are noted at top of panel. (Bottom) Percent of each solar rotation when spacecraft was within CME.

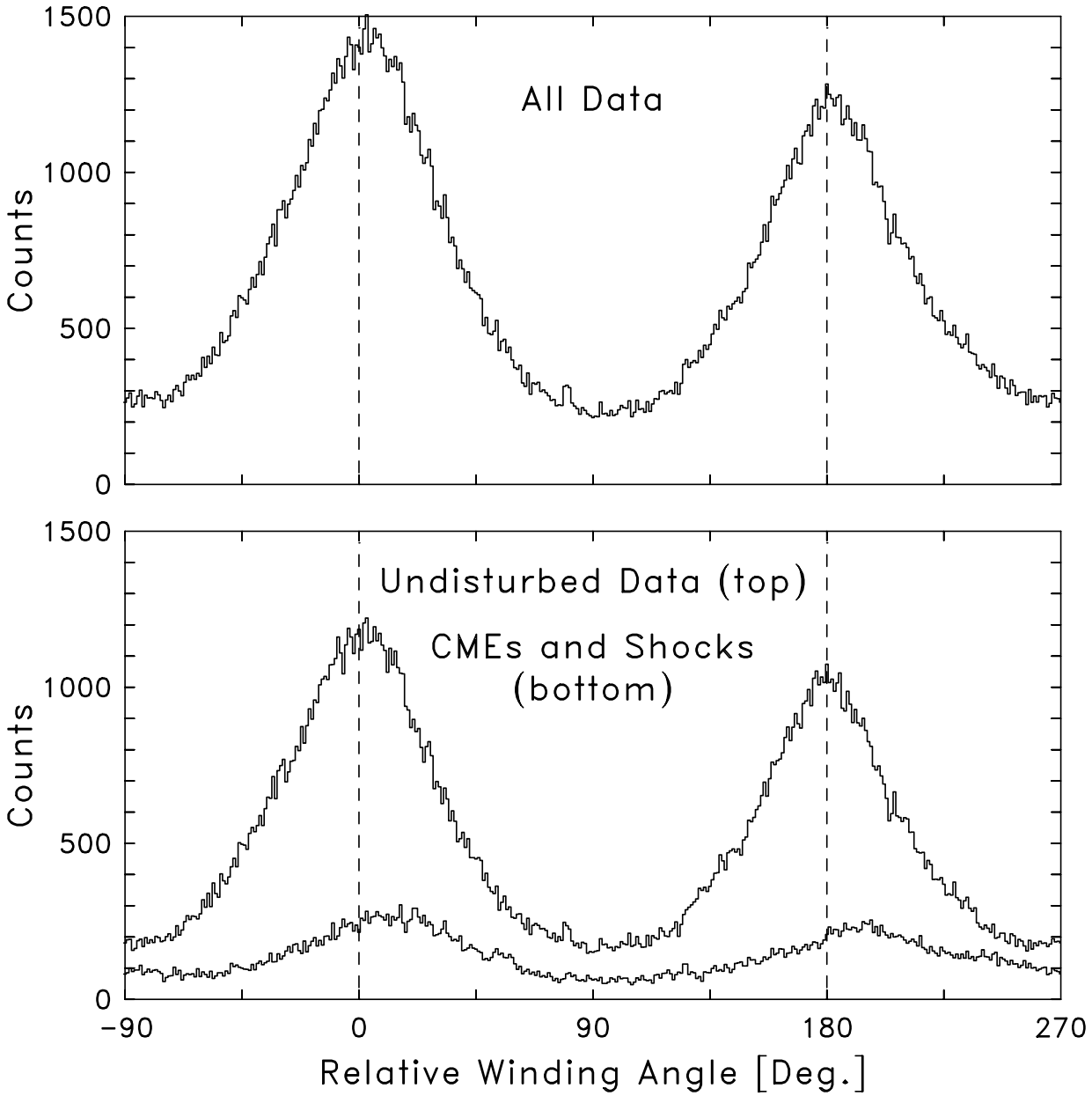


**Figure 2.** Histograms of winding angles for 5-min averaged ISEE 3 data excluding year 1980. Winding angles are plotted relative to the *Parker* [1958] prediction using the measured wind speed and 0 $R_S$ source surface. The top panel shows the full data set. The bottom panel shows distribution for undisturbed periods (top curve) and CME and postshock observations (bottom curve). Overwinding is clearly evident in the disturbance subset, while the average and most probable winding angle of the undisturbed data agrees with the Parker prediction.

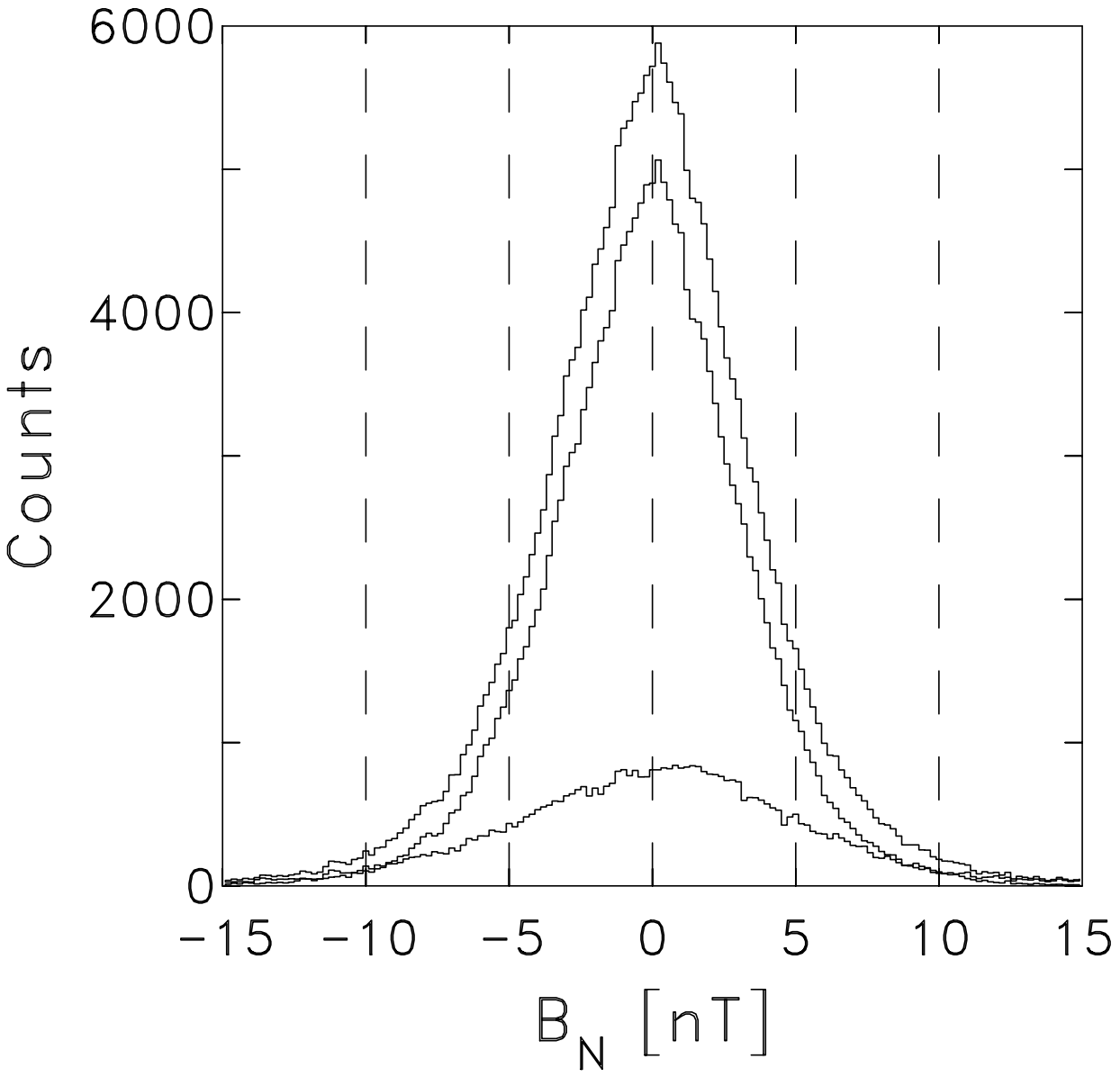


**Figure 3.** Histograms of the magnetic field N component distribution for the entire data set (top curve), for the undisturbed data as represented by CME and shock subset 2 (middle curve), and for the disturbance subset as represented by all data not contained in CME and shock subset 2 (bottom curve).

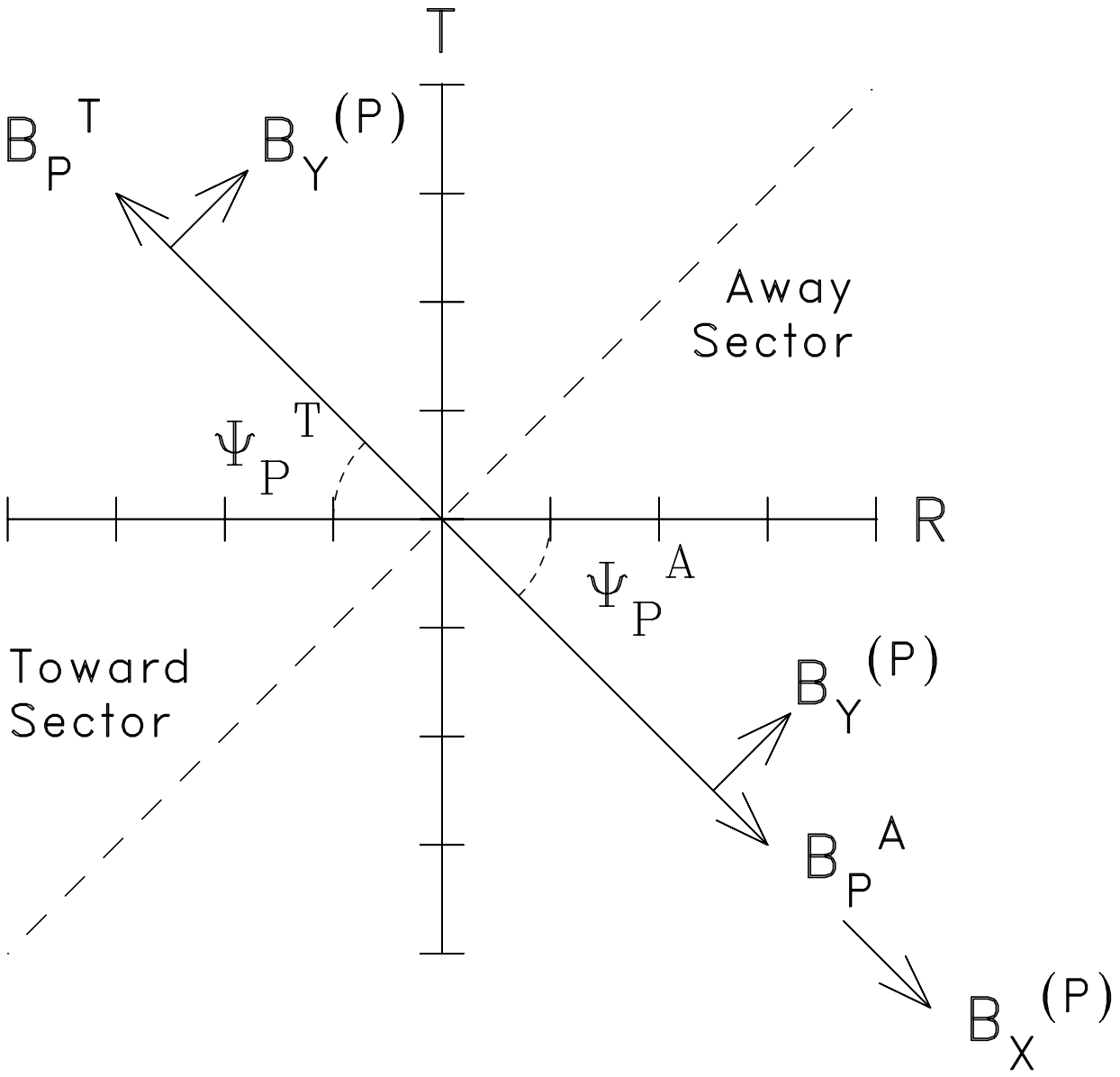


**Figure 4.** Field component definitions used by *Bieber and Rust* [1995] showing a nominal 45° winding angle. Their analyses compute the expected winding angle from the observed wind speed so that the variation relative to 45° is seen.